

Approximating the Capacitance of Square Plates; A Method of Moments Convergence Study

Samuel J. Wyss[†]

[†]School of Nuclear Engineering
Purdue University
West Lafayette, Indiana 47907
E-mail: wysss@purdue.edu

Abstract—The Method of Moments (MoM) is applied to simulate the capacitance of an arbitrarily sized square metallic plate. To model this system *in silico*, the Electrostatic Integral Equation (EIE) is used to simulate the charge distribution for a fixed potential on the metallic plate. The charge is then determined by integrating it element-wise over the surface which is then used to solve for capacitance. This procedure is used to evaluate various forms of the underlying integral equations from approximations of square elements, exact forms, to subdomain collocation. Capacitance values from these methods are first compared to data found in the literature as a verification and validation step and then compared to each other in terms of the mesh size required for these methods to achieve the same level of precision.

I. INTRODUCTION

Contrary to many other methods in Computational Electromagnetics (CEM), the Method of Moments (MoM) is purely based on the integral form of Maxwell's Equations and underlying Green's Functions [1]. In the context of the Electrostatic Integral Equation (EIE), MoM uses the potential created by individual point charges on surfaces to solve for charge density as a function of surface location. This charge distribution can trivially be integrated over surface elements to solve for the net charge on an surface for an arbitrary geometry and applied potential. From this, the capacitance of said structure can easily be obtained.

In matrix form, the EIE relates the point source response of charges in a given surface element to all other surface elements and the applied potential. The use of Green's Functions in the problem formulation allows for these problems to be solved without the need to terminate models spatially which is a common source of error in other CEM methods. However, the use of Green's Functions results in fully dense matrices, thus requiring the computational complexities and memory footprint that comes with solving them which at first may be seen as a downside of MoM. However, As these matrices only require the discretization of surfaces [1], [2] thereby resulting in much smaller system matrices overall which helps to compensate for the typical $O(n^3)$ computation complexity required to solve these dense systems.

The development and results of this work are laid out as follows. Section II contains a short derivation of the EIE from Gauss's Law followed by the setup of the EIE matrix equations for a circular approximation of square surface

elements, an exact form for surface elements, and finally the subdomain collocation. Section III contains a verification of the model with a capacitance range found in the literature, an explanation of the plate charge distribution, an analysis of the asymptotic number of operations required to determine the plate capacitance for all three methods. Finally, Section IV contains closing remarks regarding the analysis and potential future work.

II. MATHEMATICAL MODEL

To model these systems *in silico*, an appropriate mathematical model must first be derived from Maxwell's Equations. The development of said model is arranged as follows. Section II-1 contains the derivation of the EIE from Maxwell's Equations followed by surface element discretization into a simultaneous set of equations. Section II-2 outlines three formulations of the Systems matrix A starting with elements approximated as circles, an exact solution, and finally subdomain collocation.

1) *The Electrostatic Integral Equation (EIE)*: From basic electrostatics, the integral form of Gauss's Equation over some surface S is as follows

$$\iint_S \epsilon_0^{-1} g(\mathbf{r}, \mathbf{r}') \rho_s(\mathbf{r}') dS' = \Phi(r) \quad (1)$$

where ϵ_0 is the permittivity of free space, $\rho_s(\mathbf{r}')$ is the surface charge density, $\Phi(r)$ is the electrostatic potential, and $g(\mathbf{r}, \mathbf{r}')$ is the corresponding Green's function (integration kernel)

$$g(\mathbf{r}, \mathbf{r}') = \frac{1}{4\pi|\mathbf{r} - \mathbf{r}'|} \quad (2)$$

2) *System Matrix Approximations*:

III. NUMERICAL RESULTS

With the mathematical model now fully established, the implementation of this model is documented in Section III-A. From here Sections III-B verifies the model against exact dispersion relations for multiple modes in rectangular waveguides. Section III-C performs an analysis of Dispersion characteristics in circular waveguides and addresses the advantages of using FEA for this task. Finally, Section III-D compares the dispersion characteristics of the rectangular and ridged rectangular waveguides for multiple modes and discusses practical applications of ridged waveguides.

A. Implementation

All meshes used in the following sections were generated using Coreform Cubit [3] with a tutorial provided by [1]. For the rectangular waveguide found in III-B, a WR-90, X-band waveguide with $a = 0.02286\text{m}$ and $b = 0.01016\text{m}$ was used [4]. For the circular waveguide used in III-C, a similarly sized circular waveguide of radius $r = 0.01\text{m}$ was used. In order to compare the non-ridged to the ridged waveguide the same WR-90, X-band waveguide was used in Section III-D as in Section III-B; however, with two $0.0025 \times 0.0025\text{m}$ notches cut out along the long edge. Example meshes of the later two geometries can be found in Figures 1-2. These meshes were generated using Coreform Cubit's TriAdvance algorithm all containing ≈ 2000 nodes which is appropriate for the applications studied here. Coreform Cubit's `nodeset` feature was used to create a set of all nodes on the boundaries of these geometries. This allows for $O(1)$ lookups of elements on the boundary which was utilized heavily when performing TM mode analysis. These meshes were saved into the ABAQUS `.inp` ASCII format, which was chosen for its human readability which was invaluable during the development of this code.

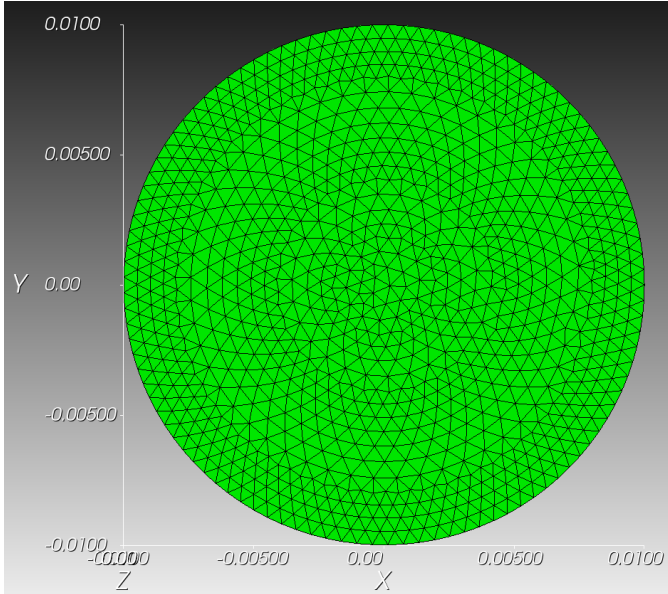


Fig. 1: Circular Waveguide Mesh used in Section III-C

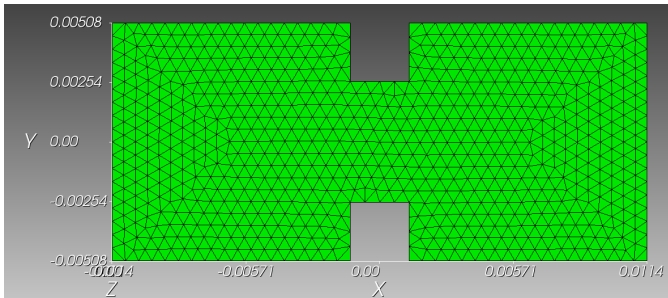


Fig. 2: Ridged Rectangular Waveguide Mesh used in Section III-D

The mathematical model outlined in Section II was implemented in Python for its general flexibility and existing numerical packages such as NumPy and SciPy which were used to solve the general eigenvalue problems established in (??-??). In addition to these packages, the MeshIO package was used as it has a built in reader for `.inp` files, allowing mesh data to be read in with ease. From this, all generated data was directly plotted using Matplotlib thereby eliminating the need to save any generated data to disk.

B. Verification and Validation

Prior to performing any kind of 'novel' analysis, the implemented model must first be benchmarked against analytic results. For this reason, the case of a WR-90, X-band waveguide with $a = 0.02286\text{m}$ and $b = 0.01016\text{m}$ is first considered [4].

In this and all following sections the spatial distributions of TE modes will be plotted. Only one mode will be plotted per section as these are merely visual aids in comparison to the dispersion charts which will contain data from the first 3 TE and TM modes. The choice of the given TE mode is entirely arbitrary and was chosen for its post processing simplicity and to ensure adequate comparisons exist in the literature [5]. The TE_{11} , H_z field distribution can be found in Fig. 3.

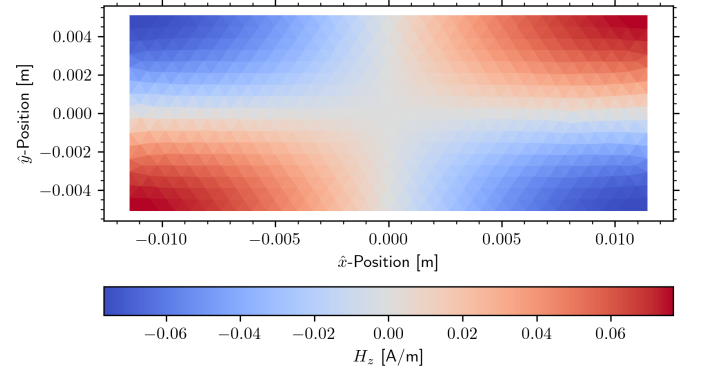


Fig. 3: TE_{11} , H_z Field Distribution in a Rectangular WR-90, X-band Waveguide

As seen in Fig. 3 the TE_{11} , H_z field profile matches that of the TE_{11} found in the literature [5] thus confirming its accuracy in recreating spatial field profiles. The TE_{10} and TE_{21} modes profiles were also vetted, however are not shown to reduce clutter.

Next, a dispersion plot of the first three TE and TM modes in this waveguide is constructed. To benchmark to theory, the following analytic cutoff wave number is used:

$$k_c = \sqrt{\left(\frac{m\pi}{a}\right)^2 + \left(\frac{n\pi}{b}\right)^2}, \quad (3)$$

where m and n are the corresponding mode propagation numbers. From this, the first three, unique, and nonzero simulated cutoff wave numbers from both the TE and TM modes were used to create the dispersion plot in Fig. 4.

As seen in Fig. 4, the dispersion relations predicted by the implemented model match that predicted by theory excellently.

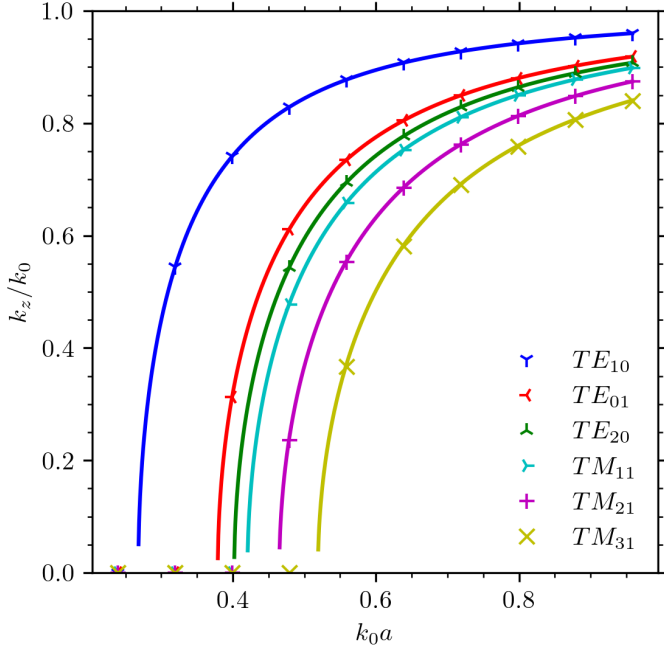


Fig. 4: Dispersion Plots of First Three TE and TM Modes in Rectangular WR-90, X-band Waveguide with Solid Lines as Analytical Results and Corresponding Markers as Simulated Results

Additionally, this demonstrates that the choice of using ≈ 2000 nodes to represent these geometries is more than sufficient to ensure convergence on the true solution. With this, more sophisticated waveguides can now be investigated knowing that the underlying mathematical model is sound.

C. Circular Waveguides

With the model successfully validated against the analytic results of a rectangular waveguide, a circular waveguide of radius $r = 0.01\text{m}$ is now assessed. One last visual verification step is performed by comparing the field profiles of the TE_{01} and TE_{11} modes generated by the model to that of the analytic profiles found in literature. The simulated TE_{01} H_z profile can be found in Fig. 5.

As seen in Fig. 5, the H_z profile matches that found in the literature [5], thereby providing additional validation for the implemented numerical model. These field plots also highlight one of the main strengths of FEM; which is its ability to work with unstructured grids out of the box. Modeling a similar profile using a finite difference method would result in egregious stair-stepping error if performed in Cartesian coordinates, or would require a special derivation in polar or cylindrical coordinates potentially limiting the model's usefulness. On the other hand, FEA is able to handle these curved geometries using unstructured grids with relative ease.

From here a similar analysis to that of Fig. 4 is performed for circular waveguides. Traditionally, producing such plots would require tables containing roots of the Bessel function

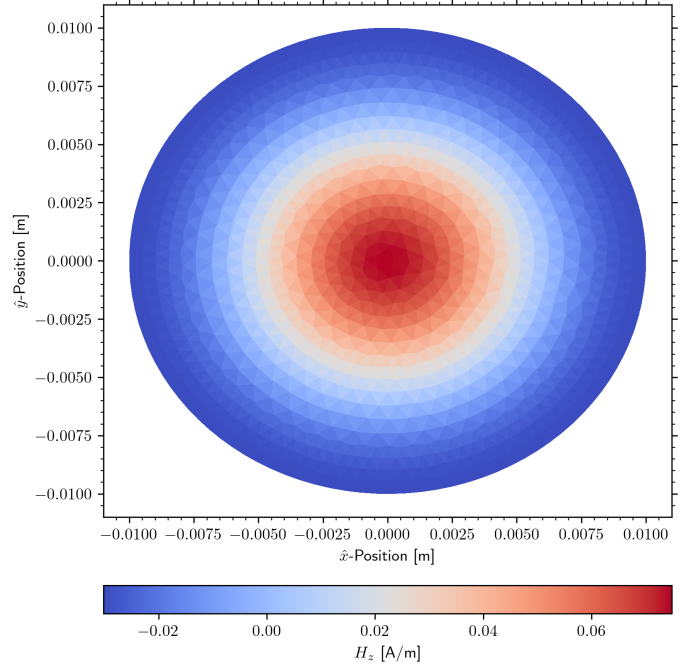


Fig. 5: TE_{01} , H_z Field Distribution in a Circular Waveguide with $r = 0.01\text{m}$

of the first kind p_{nm} and its derivative p'_{nm} which are used to determine the cutoff wave numbers as

$$k_c = \frac{p'_{nm}}{r}, \quad (4)$$

and

$$k_c = \frac{p_{nm}}{r} \quad (5)$$

respectfully for the TE and TM modes [5]. Using the above FEM, we are able to directly calculate the dispersion relations for any circular waveguide without the use of the roots of a Bessel function or its derivative. The simulated dispersion relations can be found in Fig. 6.

As seen in Fig. 6, the bandwidth between individual propagation modes in a circular waveguide is much less than that of rectangular waveguides as shown in Fig. 4. This is perhaps most notable between the TE_{11} dominant mode and the next TM_{01} mode, which is rather small. This is well documented in the literature [6] and is one of the main factors limiting circular waveguides from being used in wide-band applications. Finally, FEA was able to successfully predict the equivalence of the cutoff wave number for the TE_{01} and TM_{11} modes which is well documented in the literature [5] thereby providing one last verification step prior to considering ridged rectangular waveguides.

D. Comparison of Ridged and Non-Ridged Waveguides

With all validation steps completed, a comparison of a standard WR-90, X-band waveguide to that of a double ridged WR-90, X-band waveguide is now provided. As seen in Fig. 2, ridges are of size $0.0025 \times 0.0025\text{m}$ and are placed at the

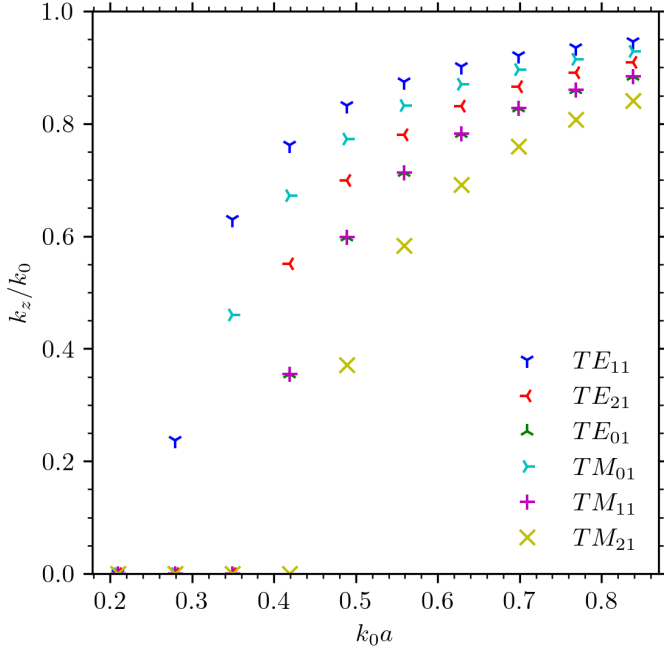


Fig. 6: Dispersion Plots of First Three TE and TM Modes in a Circular Waveguide with $r = 0.01\text{m}$

centerline of the waveguide. Similarly to Section III-B, the H_z field profile of the TE_{11} mode is assessed as shown in Fig. 7.

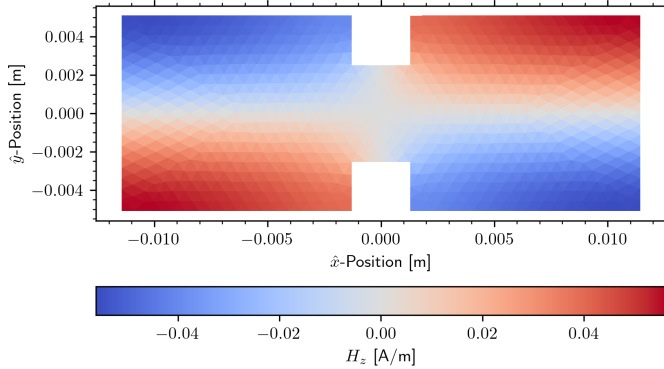


Fig. 7: TE_{11} , H_z Field Distribution in a Ridged Rectangular WR-90, X-band Waveguide

As seen in Fig. 7 the field profile is nearly identical to that of the non-ridged WR-90 waveguide shown in Fig. 3. This is expected as the propagation mode is identical despite the introduction of ridges. To demonstrate differences, a dispersion plot for this ridged waveguide is provided. To highlight discrepancies between the ridged and base waveguides, the theoretical base dispersion curves are plotted as solid lines, and the corresponding simulated data for the same modes as markers. Said plot can be found in Fig. 8.

It is clear from Fig. 8 that the cutoff wave number of the dominant TE_{10} mode is less than that of the rectangular waveguide in alignment with the theory [5]. In addition to this, all fields with cutoff wave numbers greater than the dominant mode all experience an increase in cutoff wave number within the ridged waveguide. These phenomenon can

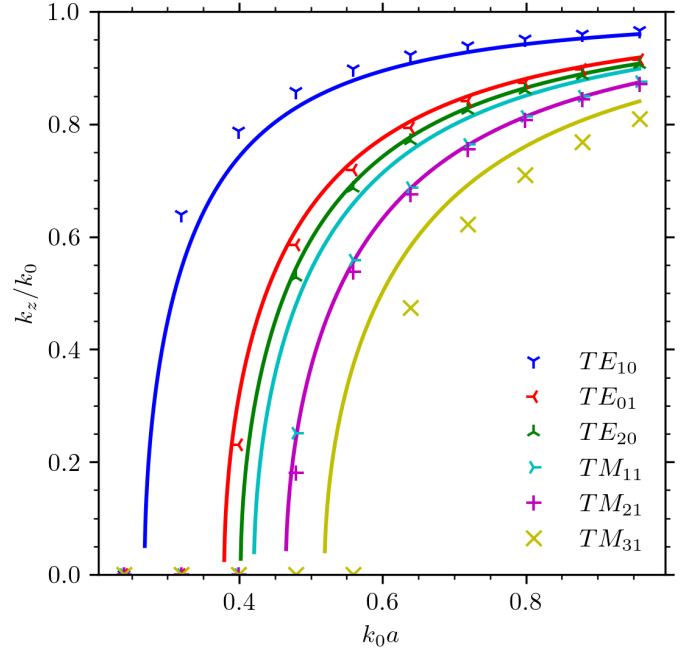


Fig. 8: TE_{11} , H_z Field Distribution in a Ridged Rectangular WR-90, X-band Waveguide with Solid Lines as the Theoretical Dispersion Relation for Base Waveguide and Corresponding Markers as Simulated Dispersion Relation for Ridged Waveguide

all be explained via field buckling caused by the inclusion of ridges. To demonstrate this, the field profiles of the dominant TE_{10} modes for both the base and ridged waveguides are plotted which can be found in Figs. 9-10.

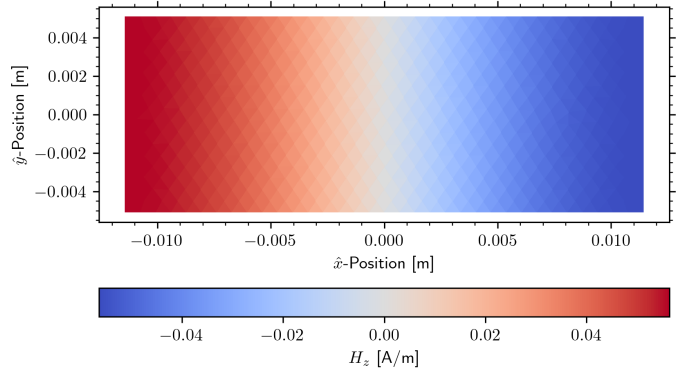


Fig. 9: Dominant TE_{10} , H_z Field Distribution in a Rectangular WR-90, X-band Waveguide

Fig. 9 shows that in the base waveguide there are two distinct regions within the TE_{10} , H_z field profile. In the case of the ridged waveguide, the ridges align with the gap between these field regions allowing for the same field profile to be achieved at lower frequencies, thus resulting in the lowering of the cutoff wave number. In other words, the inclusion of ridges facilitates a lower overall field buckling for this propagation mode. In contrast to this, higher order modes such as the TE_{11} mode found in Fig. 7 require increased

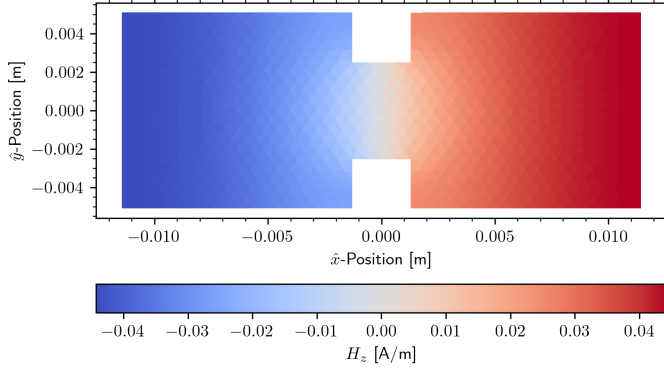


Fig. 10: Dominant TE_{10} , H_z Field Distribution in a Ridged Rectangular WR-90, X-band Waveguide

buckling in order to satisfy the boundary conditions of (??-??) to achieve the same field profile. This increased field buckling directly corresponds to an increase in the minimum cutoff wave number, and corresponding frequency content, to recreate these higher-order, more complex, propagation modes. For this reason, ridged waveguides offer superior bandwidth for the dominant modes making them superior for transmitting high-bandwidth signals.

IV. CONCLUSION

A 2-dimensional finite element method program was developed from Maxwell's Equations allowing for field distribution and dispersion analysis of arbitrarily shaped homogenous waveguides. The model was first validated against the analytic field profiles and dispersion curves for a rectangular waveguide. From here, additional verification was performed on the field profiles of circular waveguides. Next, the model was used to predict the dispersion characteristics of said circular guide which can be difficult to do analytically without tabulated

Bessel function data. Finally, the model was used to compare ridged waveguides to their non-ridged counterparts. It was shown that the inclusion of ridges significantly expands the bandwidth available to the dominant TE_{10} mode in alignment with theory. This phenomenon was explained using the change in field buckling caused by complex modes requiring higher frequencies to achieve the same field profiles where as the buckling working in the favor of simpler field profiles resulting in a lowering of the cutoff wave number.

While relatively general in the sense that the model works for any .inp input waveguide mesh, the model would benefit from increased work regarding the identification of modes which currently is done manually by the user in order to produce dispersion curves and field profile plots. The model would also benefit from using sparse matrix types as defined in SciPy as opposed to the dense NumPy arrays used in this program. In addition to this, it would be interesting to combine this model with the FDTD model developed in the last project in order to generate the field profiles of more complex waveguides for use in the TF/SF source condition. This would allow for temporal analysis of more sophisticated waveguides than the simple rectangular model used in the former project.

REFERENCES

- [1] T. E. Roth, *ECE 61800 Lecture Notes*. Purdue University, 2024.
- [2] J.-M. Jin, *Theory and Computation of Electromagnetic Fields*. John Wiley & Sons, 2011.
- [3] Coreform LLC, "Coreform cubit," <https://coreform.com/products/coreform-cubit/>, 2024, [Online; accessed 26-March-2024].
- [4] Everything RF contributors, "Rectangular waveguide sizes," <https://www.everythingrf.com/tech-resources/waveguides-sizes>, 2021, [Online; accessed 28-February-2024].
- [5] D. M. Pozar, *Microwave Engineering*. John Wiley & Sons, 2011.
- [6] Cadence System Analysis, "An introduction to circular waveguide modes," <https://resources.system-analysis.cadence.com/blog/msa2021-an-introduction-to-circular-waveguide-modes>, [Online; accessed 27-March-2024].